Check for updates

View Article Online
View Journal

Journal of
Materials Chemistry C

Accepted Manuscript

This article can be cited before page numbers have been issued, to do this please use: B. Yin, J. Cavin, D. Wang, D. Khan, M. Shen, C. Laing, R. Mishra and B. Sadtler, *J. Mater. Chem. C*, 2019, DOI: 10.1039/C8TC06470A.

This is an Accepted Manuscript, which has been through the Royal Society of Chemistry peer review process and has been accepted for publication.

Accepted Manuscripts are published online shortly after acceptance, before technical editing, formatting and proof reading. Using this free service, authors can make their results available to the community, in citable form, before we publish the edited article. We will replace this Accepted Manuscript with the edited and formatted Advance Article as soon as it is available.

You can find more information about Accepted Manuscripts in the author guidelines.

Please note that technical editing may introduce minor changes to the text and/or graphics, which may alter content. The journal's standard Terms & Conditions and the ethical guidelines, outlined in our author and reviewer resource centre, still apply. In no event shall the Royal Society of Chemistry be held responsible for any errors or omissions in this Accepted Manuscript or any consequences arising from the use of any information it contains.

ROYAL SOCIETY OF CHEMISTRY

rsc.li/materials-c

View Article Online
DOI: 10.1039/C8TC06470A

Published on 27 February 2019. Downloaded by Washington University in St. Louis on 2/27/2019 4:05:23 PM.

Fluorescence Microscopy of Single Lead Bromide Nanocrystals Reveals Sharp Transitions during Their Transformation to Methylammonium Lead Bromide

Bo Yin[1], John Cavin[2], Dong Wang[3], Daniel Khan[3], Meikun Shen[3], Craig Laing[3], Rohan Mishra[4,1], Bryce Sadtler[3,1]*

[1]Institute of Materials Science & Engineering, Washington University, St. Louis, Missouri 63130

[2]Department of Physics, Washington University, St. Louis, Missouri 63130

[3]Department of Chemistry, Washington University, St. Louis, Missouri 63130

[4]Department of Mechanical Engineering and Materials Science, Washington University, St. Louis, Missouri 63130

* To whom correspondence should be addressed. Email: sadtler@wustl.edu

Abstract

Control over the nucleation and growth of lead-halide perovskite crystals is critical to obtain semiconductor films with high quantum yields in optoelectronic devices. In this report, we use the change in fluorescence brightness to image the transformation of individual lead bromide ($PbBr_2$) nanocrystals to methylammonium lead bromide ($CH_3NH_3PbBr_3$) via intercalation of CH_3NH_3Br. Analyzing this reaction one nanocrystal at a time reveals information that is masked when the fluorescence intensity is averaged over many particles. Sharp rises in the intensity of single nanocrystals indicate they transform much faster than the time it takes for the ensemble average to transform. While the ensemble reaction rate increases with increasing CH_3NH_3Br concentration, the intensity rises for individual nanocrystals are insensitive to the CH_3NH_3Br

Journal of Materials Chemistry C Accepted Manuscript

View Article Online
DOI: 10.1039/C8TC06470A

Published on 27 February 2019. Downloaded by Washington University in St. Louis on 2/27/2019 4:05:23 PM.

concentration. To explain these observations, we propose a phase-transformation model in which the reconstructive transitions necessary to convert a $PbBr_2$ nanocrystal into $CH_3NH_3PbBr_3$ initially create a high energy barrier for ion intercalation. A critical point in the transformation occurs when the crystal adopts the perovskite phase, at which point the activation energy for further ion intercalation becomes progressively smaller. Monte Carlo simulations that incorporate this change in activation barrier into the likelihood of reaction events reproduce key experimental observations for the intensity trajectories of individual particles. The insights gained from this study may be used to further control the crystallization of $CH_3NH_3PbBr_3$ and other solution-processed semiconductors.

1. Introduction

The crystallization of solution-processed, semiconductor films plays a critical role in controlling their optoelectronic quality.[1-12] For example, polycrystalline films of lead halides (PbX_2 with X = Cl, Br, or I) transform into the corresponding methylammonium lead halide ($CH_3NH_3PbX_3$) perovskite semiconductor through the intercalation of $CH_3NH_3^+$ and X^- ions into the PbX_2 film.[8-14] This solid-state reaction occurs spontaneously when PbX_2 films are exposed to either a solution or vapor containing CH_3NH_3X, which has been used to fabricate photovoltaics and light-emitting diodes with high quantum yields.[11-17] The performance of these devices is highly dependent on the composition and mesoscale morphology of the films.[11-25] Several studies have used electron microscopy, x-ray diffraction, and optical spectroscopy to correlate the morphology and optical properties of $CH_3NH_3PbX_3$ films with growth conditions, such the reaction temperature, growth time, and the CH_3NH_3X concentration.[4-12] However, solution-processed, semiconductor films often possess heterogeneity in composition,

Journal of Materials Chemistry C Accepted Manuscript

View Article Online
DOI: 10.1039/C8TC06470A

Published on 27 February 2019. Downloaded by Washington University in St. Louis on 2/27/2019 4:05:23 PM.

crystallinity, defect concentration, and grain size. Thus, techniques that can spatially and temporally map properties such as fluorescence brightness, excited charge carrier lifetimes, photocurrent collection, and open-circuit potential are critical to gain further insight into how local structure and composition affect performance in optoelectronic devices. These techniques include photocurrent microscopy,[25] transient absorption microscopy,[26-28] and fluorescence microscopy.[29-42]

Fluorescence microscopy provides the ability to spatially map charge carrier dynamics in both polycrystalline films and nanoscale crystals of $CH_3NH_3PbX_3$.[29-42] The emission intensity and wavelength in $CH_3NH_3PbX_3$ crystals are optical signatures that can be linked with variations in composition, crystallinity, defect concentration, and the degree of quantum confinement. For instance, the fluorescence brightness in polycrystalline films of $CH_3NH_3PbI_3$ is weaker at grain boundaries,[30] and the emission wavelength red-shifts with halide composition going from X = Cl to Br to I.[31, 40] Fluorescence microscopy has also been used to observe solid-state transformations in lead-halide perovskite microcrystals in situ by monitoring changes in either the fluorescence intensity or the emission wavelength.[9, 40] Hodes and coworkers observed the appearance of multiple bright spots across the surface of a large PbI_2 (~ 50 μm) crystal upon exposure to CH_3NH_3I, indicating that many nucleation events occurred simultaneously as the crystal transformed to $CH_3NH_3PbI_3$.[9] Similarly, Tachikawa and coworkers used the shift in emission wavelength to watch ion exchange between a $CH_3NH_3PbBr_3$ microcrystal (~ 8 μm) and CH_3NH_3I in solution.[40] They also observed that the initial single crystal became polycrystalline during the transformation through the nucleation of nanoscale grains of $CH_3NH_3PbI_3$.

The observed rates of solid-state transformations in macroscopic crystals are the result of many nucleation and growth events occurring simultaneously.[10, 29, 43] Furthermore, the solid-

Journal of Materials Chemistry C Accepted Manuscript

View Article Online
DOI: 10.1039/C8TC06470A

Published on 27 February 2019. Downloaded by Washington University in St. Louis on 2/27/2019 4:05:23 PM.

state diffusion of ions can be the rate-determining step for polycrystalline films with thicknesses greater than 100 nm. For example, the interfacial reaction between CH_3NH_3I and PbI_2 at the top surface of a PbI_2 film blocks diffusion of $CH_3NH_3^+$ and I^- ions further into the film.[10] On the other hand, a nanoscale crystal can transform via a single nucleation event when its size is comparable to the critical nuclei needed for the new phase to form.[43, 44] The high surface-to-volume ratio of nanoscale crystals also facilitates rapid diffusion of ions in and out of the crystal.[45-55] By studying the reactivity and photophysics of individual nanocrystals, one can observe behavior that is obscured in the ensemble average.[36, 54-62] For example, a related solid-state transformation to the one studied in this report is cation exchange in semiconductor chalcogenide nanocrystals where cations in solution replace the cations within the nanocrystal lattice.[47-55] Using fluorescence microscopy, Routzhan and Jain observed that the conversion of individual CdSe nanocrystals to Ag_2Se via cation exchange is much faster than the time it takes for the ensemble of nanocrystals to transform.[54] Thus, the ensemble reaction rate is dictated by a population of nanocrystals that transform abruptly at different times rather than the simultaneous conversion of the entire population through multiple intermediate states.

We used fluorescence microscopy to image the conversion of single $PbBr_2$ nanocrystals to $CH_3NH_3PbBr_3$ via ion intercalation. The change in fluorescence intensity provides a signature for this reaction. While this reaction has been previously monitored in both polycrystalline films and microscale crystals,[9, 10] we obtain new insights by isolating individual nucleation and growth events among nanoscale crystallites. We observe significant differences in the reaction time and concentration dependence of individual particles compared to their ensemble average. Applying statistical analysis to these reaction trajectories, we develop a model for how the phase transformation of individual nanocrystals leads to the observed ensemble behavior.

Journal of Materials Chemistry C Accepted Manuscript

View Article Online
DOI: 10.1039/C8TC06470A

Published on 27 February 2019. Downloaded by Washington University in St. Louis on 2/27/2019 4:05:23 PM.

2. Results and Discussion

2.1 Synthesis of $PbBr_2$ Nanocrystals and Their Conversion to $CH_3NH_3PbBr_3$

Lead bromide nanocrystals were synthesized using a procedure reported by Scholes and coworkers (see the **Electronic Supplementary Information (ESI)** for details of the procedure).[63] **Figure 1a** shows a transmission electron microscopy (TEM) image of the initial $PbBr_2$ nanocrystals. The average diameter for these $PbBr_2$ nanocrystals was 3.9 ± 0.8 nm (average ± 1st standard deviation, see **Figure S1** for a histogram of nanocrystal diameters). An electron diffraction pattern measured for a cluster of nanocrystals shows a ring matching the d-spacing for the (211) planes of $PbBr_2$. While peaks in the x-ray diffraction pattern were broad, the most intense peak also matched the (211) d-spacing of $PbBr_2$ (see **Figure S2**). X-ray photoelectron spectroscopy performed on dried films of the nanocrystals indicated the presence of Pb in the +2 oxidation state and Br in the –1 oxidation state as expected for $PbBr_2$ (see **Figure S3**).

A TEM image of the product after the addition of CH_3NH_3Br to a solution of $PbBr_2$ nanocrystals is shown in **Figure 1b**. The average diameter for the final nanocrystals was 3.1 ± 0.8 nm (average ± 1st standard deviation, see **Figure S1**). Considering the larger lattice volume of $CH_3NH_3PbBr_3$ compared to $PbBr_2$, the smaller size suggests etching of the nanocrystals during the transformation. Partial dissolution of the lead halide has been previously observed when this reaction was performed on microscale crystals and in thin films.[9, 12]

We next monitored this transformation ex situ by adding varying amounts of CH_3NH_3Br (0.55 mg/mL in anhydrous isopropanol) to solutions of $PbBr_2$ nanocrystals and recording the resulting absorption and photoluminescence spectra (**Figure 2**). The absorption spectra showed

Journal of Materials Chemistry C Accepted Manuscript

View Article Online
DOI: 10.1039/C8TC06470A

Published on 27 February 2019. Downloaded by Washington University in St. Louis on 2/27/2019 4:05:23 PM.

a progressive increase in visible absorption at wavelengths from 300 to 510 nm when increasing amounts of CH_3NH_3Br were added (**Figure 2a**). After the addition of 90 μL of the CH_3NH_3Br solution, the absorption onset was 510 nm. When larger amounts of the CH_3NH_3Br solution were added, the absorption onset remained the same. However, the nanocrystals began to precipitate, which led to scattering in the absorption spectra (see dashed, orange trace in **Figure 2a**). The initial $PbBr_2$ nanocrystals were non-fluorescent, but became highly fluorescent when increasing amounts of CH_3NH_3Br were added. For different amounts of CH_3NH_3Br, the maxima in the fluorescence spectra varied between 510 and 516 nm. Both the absorption onset and fluorescence maximum of the nanocrystals are blue-shifted compared to the bulk electronic band gap of 2.3 eV (~540 nm) for $CH_3NH_3PbBr_3$.[20] Size-dependent blue-shifts have been previously observed for $CH_3NH_3PbBr_3$ and $CH_3NH_3PbI_3$ nanocrystals with dimensions smaller than ~ 5 nm. These spectral shifts have been attributed to both quantum-confinement as well as structural distortions in the crystals.[3, 35, 36, 63, 64] The progressive blue shift in the fluorescence maxima when larger amounts of CH_3NH_3Br were added (ranging from 20 to 90 μL of the CH_3NH_3Br solution) is likely due to etching of the nanocrystals as observed by TEM. In the measurements described below, we use the dramatic changes in fluorescence intensity for single nanocrystals when CH_3NH_3Br is added to monitor this reaction rather than the spectral shift of the emission band.

2.2 Single-Particle Fluorescence Trajectories

Figure 2 shows how the optical properties of the initial $PbBr_2$ nanocrystals changed after varying amounts of CH_3NH_3Br were added. However, these ensemble averages of optical signatures can mask important information about the reaction, such as whether individual nanocrystals reach the

Journal of Materials Chemistry C Accepted Manuscript

View Article Online
DOI: 10.1039/C8TC06470A

Published on 27 February 2019. Downloaded by Washington University in St. Louis on 2/27/2019 4:05:23 PM.

same stage of conversion when a given amount of reactant is added. We next used fluorescence microscopy to image the transformation of individual nanocrystals in situ. The experimental set-up is shown in **Scheme 1** and is described further in the **ESI**. Our set-up is similar to that used in previous studies by Routzahn and Jain, who monitored cation exchange between CdSe and Ag_2Se nanocrystals.[54, 55] $PbBr_2$ nanocrystals are spin-coated onto a microscope coverslip, which forms the bottom half of a flow cell. The flow cell is placed over the objective of an inverted optical microscope and is initially filled with 1-octadecene (ODE). A syringe pump is then used to introduce a solution of CH_3NH_3Br at different concentrations in ODE and t-butanol (volume ratio of 3:2) into the flow cell. Under excitation with blue light (450 to 480 nm) from a light-emitting diode sent through the objective, the initial field-of-view is dark as the $PbBr_2$ nanocrystals are transparent at these wavelengths (bottom left in **Scheme 1**). On the other hand, the $CH_3NH_3PbBr_3$ nanocrystals are highly emissive when irradiated with wavelengths below 500 nm. (bottom right in **Scheme 1**). After the introduction of CH_3NH_3Br, the conversion of individual nanocrystals is marked by the appearance of bright spots in the microscope field-of-view.

By imaging this transformation in situ, we observed that single nanocrystals turn on (i.e., become bright) on a shorter time scale compared to intensity rise for the ensemble of particles (i.e., all particles within the field-of-view). Shortly after injecting the CH_3NH_3Br solution, fluorescent spots begin to appear stochastically within the microscope field-of-view (**Figure 3a-d** and **Movie M1**). Based on the fluorescence spectra shown in **Figure 2**, we attribute the appearance of these bright spots to the formation of $CH_3NH_3PbBr_3$ nanocrystals. As seen in **Figure 3e**, the integrated intensity for all nanocrystals within field-of-view increased over a period of tens of seconds. The integrated intensity rise for the ensemble became sharper when

Journal of Materials Chemistry C Accepted Manuscript

View Article Online
DOI: 10.1039/C8TC06470A

Published on 27 February 2019. Downloaded by Washington University in St. Louis on 2/27/2019 4:05:23 PM.

the concentration of CH_3NH_3Br was increased (see **Figure S4** and **Table S1**). **Figure 3f** shows intensity trajectories for several representative particles from the same video recording. Qualitatively, the intensity rises for these individual nanocrystals occur over a few seconds. However, once the solution of CH_3NH_3Br was introduced, the time it took for each nanocrystal to turn on varied. These two features of the single-nanocrystal trajectories are analyzed in more detail below. Importantly, the time point at which a nanocrystal became bright did not depend on its location in the field-of-view (see **Figure S5**). Furthermore, we used a low irradiance (~ 155 $\mu W\text{-}cm^{-2}$ near the focal plane) to avoid photodamage to the nanocrystals, and our observations did not change when a higher light intensity was used (see **Figure S8**). The combination of abrupt switching in fluorescence intensity for individual nanocrystals and the wide distribution of waiting times before they start to become bright produces the slow rise in the integrated intensity over the entire field-of-view.

To quantify differences in behavior of individual nanocrystals, we define the waiting time as the time it takes for the intensity of a single nanocrystal to reach a value above a threshold intensity once the CH_3NH_3Br solution has been added (see **ESI** for further details). Since it is experimentally difficult to know when the CH_3NH_3Br solution reaches the field-of-view, the waiting time for each nanocrystal was measured relative to the time the first nanocrystal was observed to turn on. The relative waiting times for hundreds of nanocrystals at different concentrations of CH_3NH_3Br ranging from 0.2 to 1.0 mg/mL in ODE/t-butanol are plotted in **Figure 4**. When the concentration of CH_3NH_3Br was lower than 0.2 mg/mL, we did not observe transformation of the nanocrystals, and CH_3NH_3Br was not soluble in the ODE/t-butanol solution at concentrations greater than 1.0 mg/mL. These histograms show that the distributions of waiting times become narrower as the concentration of CH_3NH_3Br increases. Furthermore, at

Journal of Materials Chemistry C Accepted Manuscript

View Article Online
DOI: 10.1039/C8TC06470A

Published on 27 February 2019. Downloaded by Washington University in St. Louis on 2/27/2019 4:05:23 PM.

higher concentrations of CH_3NH_3Br, the distributions shift towards shorter waiting times, reflecting faster ensemble kinetics. An additional histogram of waiting times using 0.3 mg/mL of CH_3NH_3Br is shown in **Figure S6**. Gaussian fits to the histograms are shown in **Figure S7**.

We next characterized the sharpness of the intensity rise for individual nanocrystals and its dependence on the CH_3NH_3Br concentration. The increase in intensity for each nanocrystal was fit to a sigmoidal function, and a switching time, τ, was extracted from this fit (see **Figure 5a**). A sharper rise in intensity will lead to a smaller value of τ (see the **ESI** for further details). **Table S1** in the **ESI** compares the intensity rise for the ensemble of nanocrystals to the average single-nanocrystal switching time at different concentrations of CH_3NH_3Br. While the ensemble intensity rise increases more rapidly at higher concentrations of CH_3NH_3Br, the average switching times are insensitive to the CH_3NH_3Br concentration. The average switching times are plotted as a function of CH_3NH_3Br concentration in **Figure 5b** along with the median relative waiting times at the same concentrations. The distributions of waiting times become narrower and shift towards shorter waiting times for higher concentrations of CH_3NH_3Br (see **Figure 4** and **Figure S7**). Thus, the median waiting time decreases with increasing CH_3NH_3Br concentration until it becomes dominated by the switching time. The short time scale of the switching time for individual nanocrystals relative to the ensemble intensity rise and its independence from reactant concentration appear to be characteristic features for this solid-state reaction. Because the diffusion coefficients of ions within the nanocrystal lattice are orders of magnitude lower than those of ions in solution,[65, 66] concentration gradients in solution due to depletion of ions near the nanocrystal surface are expected to be negligible (see the **ESI** for further discussion). In the model developed below we consider the roles of solid-state diffusion

Journal of Materials Chemistry C Accepted Manuscript

View Article Online
DOI: 10.1039/C8TC06470A

Published on 27 February 2019. Downloaded by Washington University in St. Louis on 2/27/2019 4:05:23 PM.

and the phase transformation that must occur for the nanocrystal to adopt the $CH_3NH_3PbBr_3$ structure and their effect on the resulting waiting and switching times.

2.3 Phase Transformation Model for $PbBr_2$ to $CH_3NH_3PbBr_3$ Conversion

We used Monte Carlo methods to simulate the kinetics of ion intercalation (i.e., $CH_3NH_3^+$ and Br^-) into $PbBr_2$ nanocrystals and their transformation to $CH_3NH_3PbBr_3$. These simulations involve the discrete time evolution of an ensemble of nanocrystals in the presence of a reservoir of external ions. At each time step, the probability for successful intercalation in a randomly chosen particle depends upon the free energy change, ΔG_i, associated with the i^{th} intercalation event for that particle. The dependence of the free energy and corresponding probability on the number of previous intercalation events that have taken place in the particle were varied to simulate different models for the transformation of the nanocrystal. **Figure S9** shows the change in ΔG_i and the corresponding probability, p_i for intercalation as a function of intercalation events, i. The results for two of these models are shown in **Figure 6**, which include the ensemble-averaged and representative single-particle trajectories for ion intercalation along with insets showing the distributions of simulated waiting times. In the diffusion-limited model, ΔG_i for each intercalation event is assumed to be governed by solid-state diffusion and is constant throughout the simulation (**Figure 6a, c**). This model produces switching times for single nanocrystals that occur on the same time scale as the corresponding ensemble trajectory, which is not observed experimentally. Additionally, all of the trajectories in the diffusion-limited simulations show a negative curvature at all times whereas the experimental trajectories start with a positive curvature before reaching a knee curve.

Journal of Materials Chemistry C Accepted Manuscript

View Article Online
DOI: 10.1039/C8TC06470A

Published on 27 February 2019. Downloaded by Washington University in St. Louis on 2/27/2019 4:05:23 PM.

The model shown in **Figure 6b, d** incorporates the reconstructive transitions that are necessary due to the different arrangements of Pb^{2+} and Br^- ions in the initial and final crystals. The Pb^{2+} ions in $PbBr_2$ possess a buckled arrangement (similar to phosphorene) when viewed along the [010] direction, and the $PbBr_7$ heptahedra in $PbBr_2$ are both edge and corner sharing. In $CH_3NH_3PbBr_3$, the $PbBr_6$ octahedra are connected via corner sharing to give a Pb^{2+} sublattice with a simple cubic arrangement. To model the conversion between these two crystals, ion intercalation is assumed to be diffusion-limited until a critical point after which the perovskite phase is adopted. After the phase transformation, the presence of many $CH_3NH_3^+$ and Br^- vacancy sites in the perovskite structure is expected to favor additional ion intercalation. In our simulations for this phase-transformation model, ΔG_i and the associated probability for each ion intercalation events are initially constant. After a critical number of successful events has occurred for a given particle, the value of ΔG_i for further intercalation progressively decreases. The simulations resulting from this phase-transformation model reproduce several features of the experimental fluorescence trajectories. Abrupt changes in the number of ions incorporated lead to switching times for individual trajectories that occur on a shorter time scale than the ensemble trajectory. The simulated trajectories also have the same general curvature profile as the experimental results. **Figure S10** shows histograms of the waiting times from simulations with different initial equilibrium constants using the phase-transformation model. Varying the equilibrium constant for ion intercalation in the simulations corresponds to changing the concentration of the CH_3NH_3Br solution. Comparing the experimental histograms of waiting times in **Figure 4** with the simulated ones in **Figure S10**, both show similar decreases in the medians and the widths of the waiting time distributions with increasing reactant concentration. Furthermore, in the phase-transformation model the median switching times are relatively

Journal of Materials Chemistry C Accepted Manuscript

View Article Online
DOI: 10.1039/C8TC06470A

Published on 27 February 2019. Downloaded by Washington University in St. Louis on 2/27/2019 4:05:23 PM.

insensitive to the initial equilibrium constant compared to the median switching times obtained from the diffusion-limited model (see **Figure S11**).

We investigated other models to simulate the abrupt switching times observed for individual nanocrystals. **Figure S12** in the **ESI** shows the ensemble trajectories, representative single-particle trajectories, and histograms of waiting times for three additional models that exhibit different degrees of cooperativity between intercalation events. The key feature of each of these models is that the probability for successive intercalation events for a particle increases (either continuously or abruptly) over the course of the trajectory (see **ESI** for additional details on these models). One of these models was originally proposed by Routzahn and Jain to describe cation exchange in CdSe nanocrystals with Ag^+.[54] In this positive-cooperativity model, the activation energy for each exchange event decreases linearly with the number of successful events, such that the probability for exchange increases exponentially during the simulation (see **Figure S9**). All three reaction models exhibit abrupt increases in the number of ions incorporated for individual particles that simulate the sharp changes in fluorescence intensity observed experimentally. They also show a distribution of waiting times such that the corresponding ensemble trajectory occurs over a longer time scale than the individual trajectories.

2.4 Comparison of Ion Intercalation and Cation Exchange

Previously, Routzahn and Jain studied the interconversion between CdSe and Ag_2Se nanocrystals via cation exchange using single-nanocrystal fluorescence microscopy (CdSe is fluorescent while Ag_2Se is non-fluorescent under visible excitation).[54, 55] Similar to our observations, the distribution of waiting times for fluorescent CdSe nanocrystals to turn off during cation exchange with Ag^+ narrowed as the concentration of $AgNO_3$ was increased. Furthermore, the

Journal of Materials Chemistry C Accepted Manuscript

View Article Online
DOI: 10.1039/C8TC06470A

Published on 27 February 2019. Downloaded by Washington University in St. Louis on 2/27/2019 4:05:23 PM.

average switching times were insensitive to Ag^+ concentration. However, the average switching times for fluorescence decay in CdSe to Ag_2Se conversion (determined via similar sigmoidal fitting to that shown in **Figure 5a**) were significantly shorter (on the order of hundreds of milliseconds) than our switching times. We note that while changes in fluorescence intensity provide a signature for these reactions, there is not a one-to-one correspondence between the start of the reaction and the point at which the fluorescence intensity starts to rise or fall. For example, it has been shown that interstitial Ag^+ ions in CdSe nanocrystals significantly lower the quantum yield of the nanocrystals.[52] Thus, the fluorescence turn-off during cation exchange of a CdSe nanocrystal with Ag^+ may occur at an early time point during the reaction. Consistent with this picture, the switching times for fluorescence turn-on are longer when Ag_2Se nanocrystals are converted back to CdSe. Similarly, defects reduce the emission intensity in films of $CH_3NH_3PbI_3$.[30] During the intercalation of $CH_3NH_3^+$ and Br^- ions into the $PbBr_2$ lattice, the nanocrystals may not start to emit until structural defects that quench fluorescence have been annealed.

The observed blinking of the nanocrystals following the initial intensity rise (see **Movie M1**) likely results from defects that temporarily quench the fluorescence emission as has been seen previously for $CH_3NH_3PbBr_3$ and other semiconductor nanocrystals.[34-38, 57-60] Most previous studies that have measured the on- and off-times for fluorescence blinking have used nanocrystals that were dried on a substrate. In our experiments, under continuous flow of the CH_3NH_3Br solution needed for the transformation, the fluorescence emission from the nanocrystals becomes permanently quenched after a few hundred seconds, which likely results from dissolution of the nanocrystals.[9, 12] To correlate the switching and waiting times of nanocrystals with their blinking statistics we are currently working to further stabilize the

Journal of Materials Chemistry C Accepted Manuscript

View Article Online
DOI: 10.1039/C8TC06470A

Published on 27 February 2019. Downloaded by Washington University in St. Louis on 2/27/2019 4:05:23 PM.

fluorescence emission by changing the solvent system and ligands used to passivate the nanocrystals.

Both cation exchange in chalcogenide nanocrystals and ion intercalation in lead halide nanocrystals can be described by a model in which the successive ion exchange/intercalation events become more favorable as the reaction proceeds. We hypothesize that the reason these two systems exhibit similar behavior arises from the solid-state immiscibility between the initial and final crystals. In cation exchange, the chalcogenide sublattice must also undergo significant rearrangements to accommodate the entering cations. The selenium ions have a hexagonal arrangement in CdSe while they possess an orthorhombic arrangement in Ag_2Se.[47] The immiscibility between the initial and final crystals requires the new phase to first nucleate within the crystal. In the nanoscale crystals studied here a single nucleation event likely takes place in each crystal.[43, 44] Our simulations support an initially large activation barrier for this nucleation event, followed by a decrease in activation barrier once nucleation has occurred. Furthermore, this model suggests that solid-state reactions in which there is high miscibility between the initial and final crystals should exhibit different behavior. Routzahn and Jain proposed cation exchange of CdSe nanocrystals with Hg^{2+} as one such system that exhibits high miscibility between CdSe and HgSe.[51, 54] Similarly, during anion exchange of lead-halide perovskites, the Pb^{2+} cations undergo relatively small rearrangements to accommodate halide ions (Cl^-, Br^- or I^-) of different sizes.[31, 45, 46] We expect that both the waiting and switching times for anion exchange will depend on halide concentration, and we are currently extending our single-nanocrystal fluorescence measurements to study this reaction.

Journal of Materials Chemistry C Accepted Manuscript

View Article Online
DOI: 10.1039/C8TC06470A

Published on 27 February 2019. Downloaded by Washington University in St. Louis on 2/27/2019 4:05:23 PM.

3. Conclusions

Using fluorescence microscopy, we imaged the conversion of $PbBr_2$ nanocrystals to $CH_3NH_3PbBr_3$ at the single-nanocrystal level. The nanocrystals exhibit a characteristic switching time for this reaction that is insensitive to the reactant concentration. A distribution of waiting times before each nanocrystal becomes bright leads to ensemble kinetics that are concentration dependent and much slower than the sharp transitions observed for single nanocrystals. To account for these observations, we developed a phase-transformation model that incorporates a discontinuous change in probability for ion intercalation associated with stabilizing the perovskite phase before the reaction becomes favorable. By imaging solid-state transformations in individual nanoscale crystallites, one can obtain information that is masked in the ensemble kinetics. Notably, when the overall reaction is 50% complete, the ensemble of nanocrystals consists of two populations; half of the nanocrystals are fully transformed while the other half have not yet reacted. In classical models for nucleation and growth, the nucleation rate increases with increasing concentration such that a larger number of smaller grains are formed at higher concentrations.[10] Our findings imply that the concentration dependence for the distribution of nucleation times imposes a fundamental limit to the dispersity in crystallite size when this solid-state reaction is performed in lead halide films. Tracking nanoscale chemistry with single-particle fluorescence can be applied to other reactions where there is either a change in the brightness or the spectral position of the emission from the nanocrystal, such as oxidation and ligand exchange.[67, 68]

Associated content.

Journal of Materials Chemistry C Accepted Manuscript

View Article Online
DOI: 10.1039/C8TC06470A

Electronic Supplementary Information: Materials and Methods, Supplementary Discussion, Supplementary Figures and Table, and Supplementary References.

Author information.

***email:** sadtler@wustl.edu

Conflicts of interest. There are no conflicts of interest to declare.

Acknowledgements.

This material is based upon work supported by the National Science Foundation under CHE-1753344. J.C. and R.M. acknowledge NSF for support through DMREF-1729787 and DMR-1806147, respectively. Electron microscopy and x-ray photoelectron spectroscopy were performed at the Institute of Materials Science & Engineering at Washington University. X-ray diffraction was performed in the Department of Earth and Planetary Sciences at Washington University. B. Wieliczka and R. Loomis are acknowledged for use of their absorption spectrometer.

Figure Captions

Figure 1. TEM images of (a) the initial $PbBr_2$ nanocrystals and (b) resulting $CH_3NH_3PbBr_3$ nanocrystals after reaction with CH_3NH_3Br. The inset (a) shows an electron diffraction pattern for a cluster of $PbBr_2$ nanocrystals. The bright ring corresponds to the d-spacing for the (211) plane of $PbBr_2$. The scale bar of 50 nm applies to both images.

Published on 27 February 2019. Downloaded by Washington University in St. Louis on 2/27/2019 4:05:23 PM.

Journal of Materials Chemistry C Accepted Manuscript

View Article Online
DOI: 10.1039/C8TC06470A

Published on 27 February 2019. Downloaded by Washington University in St. Louis on 2/27/2019 4:05:23 PM.

Figure 2. Optical spectra showing the conversion of $PbBr_2$ nanocrystals to $CH_3NH_3PbBr_3$. (a) Absorption spectra of the nanocrystals after the addition of increasing amounts of CH_3NH_3Br. (b) Photoluminescence spectra of the nanocrystals after the addition of increasing amounts of CH_3NH_3Br. The excitation wavelength was 400 nm for all samples except for the 90 μL aliquot in which the excitation wavelength was increased to 475 nm to reduce the emission intensity.

Scheme 1. Experimental Configuration Used to Observe the Transformation of Single $PbBr_2$ Nanocrystals to $CH_3NH_3PbBr_3$.[a]

[a] Upon excitation with blue light (450 to 480 nm), the initial $PbBr_2$ nanocrystals are non-fluorescent while the product $CH_3NH_3PbBr_3$ nanocrystals are highly fluorescent. A schematic of the microscope field-of-view is shown at the bottom. Black dots represent $PbBr_2$ nanocrystals, and green dots represent $CH_3NH_3PbBr_3$ nanocrystals after the transformation. ODE = 1-octadecene.

Figure 3. Imaging the transformation of single $PbBr_2$ nanocrystals to $CH_3NH_3PbBr_3$. (a-d) Selected frames from a video recording of the fluorescence intensity under excitation with blue light and using a CH_3NH_3Br concentration of 0.4 mg/mL. The first frame (0.0 sec) corresponds to the time when the first fluorescent spot appeared. The contrast of the images has been inverted. The scale bar shown in (a) is 5 μm and applies to all four images. (e) The integrated intensity versus time over the entire field-of-view for the same recording. (f) Intensity trajectories for individual nanocrystals from the same recording.

Journal of Materials Chemistry C Accepted Manuscript

View Article Online
DOI: 10.1039/C8TC06470A

Published on 27 February 2019. Downloaded by Washington University in St. Louis on 2/27/2019 4:05:23 PM.

Figure 4. Histograms of the relative waiting times for $PbBr_2$ nanocrystals to transform into $CH_3NH_3PbBr_3$ when the concentration of CH_3NH_3Br was (a) 0.2 mg/mL, (b) 0.4 mg/mL, (c) 0.5 mg/mL, and (d) 1.0 mg/mL. For each histogram, a relative waiting time of 0 seconds corresponds to the first nanocrystal to transform among the population. The **ESI** describes how histograms were aligned when multiple videos were recorded at the same concentration.

Figure 5. (a) Representative intensity trajectory (black trace) for a single nanocrystal and the fitting (red line) of the intensity rise to a sigmoidal function. This fitting was used to determine the switching time, τ. (b) The average switching time (black squares) and the median relative waiting time (red circles) for the conversion of $PbBr_2$ nanocrystals using different CH_3NH_3Br concentrations. The error bars for the average switching times correspond to one standard deviation.

Figure 6. Monte Carlo simulations of ion intercalation in $PbBr_2$ nanocrystals. Ensemble reaction trajectories for the (a) diffusion-limited and (b) phase-transformation models described in the text. The insets show histograms of the waiting times for individual trajectories using these models. Representative single-particle trajectories for the (c) diffusion-limited and (d) phase-transformation models.

Journal of Materials Chemistry C Accepted Manuscript

View Article Online
DOI: 10.1039/C8TC06470A

Published on 27 February 2019. Downloaded by Washington University in St. Louis on 2/27/2019 4:05:23 PM.

Table of Contents Entry

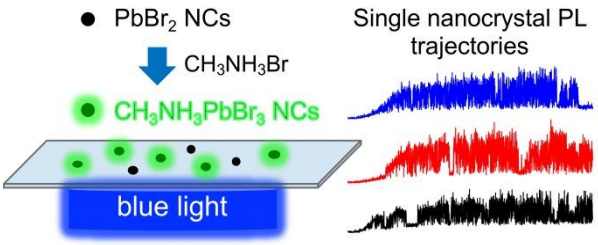

Single-nanocrystal fluorescence microscopy reveals that the immiscibility between $PbBr_2$ $CH_3NH_3PbBr_3$ crystals imposes the limiting energetic barrier for nanocrystal conversion.

References

1. T. Baikie, Y. Fang, J. M. Kadro, M. Schreyer, F. Wei, S. G. Mhaisalkar, M. Graetzel and T. J. White, *Journal of Materials Chemistry A*, 2013, **1**, 5628-5641.
2. C. C. Stoumpos, C. D. Malliakas and M. G. Kanatzidis, *Inorganic Chemistry*, 2013, **52**, 9019-9038.
3. J. J. Choi, X. Yang, Z. M. Norman, S. J. L. Billinge and J. S. Owen, *Nano Letters*, 2014, **14**, 127-133.
4. Y. Tidhar, E. Edri, H. Weissman, D. Zohar, G. Hodes, D. Cahen, B. Rybtchinski and S. Kirmayer, *Journal of the American Chemical Society*, 2014, **136**, 13249-13256.
5. G. Grancini, S. Marras, M. Prato, C. Giannini, C. Quarti, F. De Angelis, M. De Bastiani, G. E. Eperon, H. J. Snaith, L. Manna and A. Petrozza, *The Journal of Physical Chemistry Letters*, 2014, **5**, 3836-3842.
6. Y. Zhou, O. S. Game, S. Pang and N. P. Padture, *The Journal of Physical Chemistry Letters*, 2015, **6**, 4827-4839.
7. M. V. Morrell, X. He, G. Luo, A. S. Thind, T. A. White, J. A. Hachtel, A. Y. Borisevich, J.-C. Idrobo, R. Mishra and Y. Xing, *ACS Applied Nano Materials*, 2018, **1**, 6091-6098.

Journal of Materials Chemistry C Accepted Manuscript

View Article Online
DOI: 10.1039/C8TC06470A

Published on 27 February 2019. Downloaded by Washington University in St. Louis on 2/27/2019 4:05:23 PM.

8. S. Yang, Y. C. Zheng, Y. Hou, X. Chen, Y. Chen, Y. Wang, H. Zhao and H. G. Yang, *Chemistry of Materials*, 2014, **26**, 6705-6710.

9. T. M. Brenner, Y. Rakita, Y. Orr, E. Klein, I. Feldman, M. Elbaum, D. Cahen and G. Hodes, *Chemistry of Materials*, 2016, **28**, 6501-6510.

10. H. Ko, D. H. Sin, M. Kim and K. Cho, *Chemistry of Materials*, 2017, **29**, 1165-1174.

11. Q. Chen, H. Zhou, Z. Hong, S. Luo, H.-S. Duan, H.-H. Wang, Y. Liu, G. Li and Y. Yang, *Journal of the American Chemical Society*, 2014, **136**, 622-625.

12. Y. Fu, F. Meng, M. B. Rowley, B. J. Thompson, M. J. Shearer, D. Ma, R. J. Hamers, J. C. Wright and S. Jin, *Journal of the American Chemical Society*, 2015, **137**, 5810-5818.

13. J. Burschka, N. Pellet, S.-J. Moon, R. Humphry-Baker, P. Gao, M. K. Nazeeruddin and M. Grätzel, *Nature*, 2013, **499**, 316-319.

14. J.-W. Lee and N.-G. Park, *MRS Bulletin*, 2015, **40**, 654-659.

15. H. J. Snaith, *The Journal of Physical Chemistry Letters*, 2013, **4**, 3623-3630.

16. L. Zuo, S. Dong, N. De Marco, Y.-T. Hsieh, S.-H. Bae, P. Sun and Y. Yang, *Journal of the American Chemical Society*, 2016, **138**, 15710-15716.

17. L. Meng, E.-P. Yao, Z. Hong, H. Chen, P. Sun, Z. Yang, G. Li and Y. Yang, *Advanced Materials*, 2017, **29**, 1603826.

18. M. M. Lee, J. Teuscher, T. Miyasaka, T. N. Murakami and H. J. Snaith, *Science*, 2012, **338**, 643-647.

19. M. Liu, M. B. Johnston and H. J. Snaith, *Nature*, 2013, **501**, 395-398.

20. E. Edri, S. Kirmayer, D. Cahen and G. Hodes, *The Journal of Physical Chemistry Letters*, 2013, **4**, 897-902.

Journal of Materials Chemistry C Accepted Manuscript

View Article Online
DOI: 10.1039/C8TC06470A

Published on 27 February 2019. Downloaded by Washington University in St. Louis on 2/27/2019 4:05:23 PM.

21. M. Saliba, K. W. Tan, H. Sai, D. T. Moore, T. Scott, W. Zhang, L. A. Estroff, U. Wiesner and H. J. Snaith, *The Journal of Physical Chemistry C*, 2014, **118**, 17171-17177.

22. N. J. Jeon, J. H. Noh, Y. C. Kim, W. S. Yang, S. Ryu and S. I. Seok, *Nature Materials*, 2014, **13**, 897-903.

23. N. J. Jeon, J. H. Noh, W. S. Yang, Y. C. Kim, S. Ryu, J. Seo and S. I. Seok, *Nature*, 2015, **517**, 476-480.

24. L. Zhao, Y.-W. Yeh, N. L. Tran, F. Wu, Z. Xiao, R. A. Kerner, Y. L. Lin, G. D. Scholes, N. Yao and B. P. Rand, *ACS Nano*, 2017, **11**, 3957-3964.

25. S. Y. Leblebici, L. Leppert, Y. Li, S. E. Reyes-Lillo, S. Wickenburg, E. Wong, J. Lee, M. Melli, D. Ziegler, D. K. Angell, D. F. Ogletree, Paul D. Ashby, F. M. Toma, J. B. Neaton, I. D. Sharp and A. Weber-Bargioni, *Nature Energy*, 2016, **1**, 16093.

26. M. J. Simpson, B. Doughty, B. Yang, K. Xiao and Y.-Z. Ma, *The Journal of Physical Chemistry Letters*, 2016, **7**, 1725-1731.

27. Z. Guo, Y. Wan, M. Yang, J. Snaider, K. Zhu and L. Huang, *Science*, 2017, **356**, 59-62.

28. S. Nah, B. Spokoyny, C. Stoumpos, C. M. M. Soe, M. Kanatzidis and E. Harel, *Nature Photonics*, 2017, **11**, 285-288.

29. S. Ahmad, P. K. Kanaujia, W. Niu, J. J. Baumberg and G. Vijaya Prakash, *ACS Applied Materials & Interfaces*, 2014, **6**, 10238-10247.

30. D. W. de Quilettes, S. M. Vorpahl, S. D. Stranks, H. Nagaoka, G. E. Eperon, M. E. Ziffer, H. J. Snaith and D. S. Ginger, *Science*, 2015, **348**, 683-686.

31. N. Pellet, J. Teuscher, J. Maier and M. Grätzel, *Chemistry of Materials*, 2015, **27**, 2181-2188.

Journal of Materials Chemistry C Accepted Manuscript

View Article Online
DOI: 10.1039/C8TC06470A

Published on 27 February 2019. Downloaded by Washington University in St. Louis on 2/27/2019 4:05:23 PM.

32. X. Wen, R. Sheng, A. W. Y. Ho-Baillie, A. Benda, S. Woo, Q. Ma, S. Huang and M. A. Green, *The Journal of Physical Chemistry Letters*, 2014, **5**, 3849-3853.

33. S. Chen, X. Wen, J. S. Yun, S. Huang, M. Green, N. J. Jeon, W. S. Yang, J. H. Noh, J. Seo, S. I. Seok and A. Ho-Baillie, *ACS Applied Materials & Interfaces*, 2017, **9**, 6072-6078.

34. X. Wen, A. Ho-Baillie, S. Huang, R. Sheng, S. Chen, H.-c. Ko and M. A. Green, *Nano Letters*, 2015, **15**, 4644-4649.

35. F. Zhu, L. Men, Y. Guo, Q. Zhu, U. Bhattacharjee, P. M. Goodwin, J. W. Petrich, E. A. Smith and J. Vela, *ACS Nano*, 2015, **9**, 2948-2959.

36. T. Tachikawa, I. Karimata and Y. Kobori, *The Journal of Physical Chemistry Letters*, 2015, **6**, 3195-3201.

37. Y. Tian, A. Merdasa, M. Peter, M. Abdellah, K. Zheng, C. S. Ponseca, T. Pullerits, A. Yartsev, V. Sundström and I. G. Scheblykin, *Nano Letters*, 2015, **15**, 1603-1608.

38. A. Merdasa, Y. Tian, R. Camacho, A. Dobrovolsky, E. Debroye, E. L. Unger, J. Hofkens, V. Sundström and I. G. Scheblykin, *ACS Nano*, 2017, **11**, 5391-5404.

39. D. Täuber, A. Dobrovolsky, R. Camacho and I. G. Scheblykin, *Nano Letters*, 2016, **16**, 5087-5094.

40. I. Karimata, Y. Kobori and T. Tachikawa, *The Journal of Physical Chemistry Letters*, 2017, **8**, 1724-1728.

41. D. W. deQuilettes, S. Jariwala, S. Burke, M. E. Ziffer, J. T. W. Wang, H. J. Snaith and D. S. Ginger, *ACS Nano*, 2017, **11**, 11488-11496.

42. B. A. Rosales, M. P. Hanrahan, B. W. Boote, A. J. Rossini, E. A. Smith and J. Vela, *ACS Energy Letters*, 2017, **2**, 906-914.

Journal of Materials Chemistry C Accepted Manuscript

View Article Online
DOI: 10.1039/C8TC06470A

Published on 27 February 2019. Downloaded by Washington University in St. Louis on 2/27/2019 4:05:23 PM.

43. C.-C. Chen, A. B. Herhold, C. S. Johnson and A. P. Alivisatos, *Science*, 1997, **276**, 398-401.

44. K. Jacobs, D. Zaziski, E. C. Scher, A. B. Herhold and A. Paul Alivisatos, *Science*, 2001, **293**, 1803-1806.

45. G. Nedelcu, L. Protesescu, S. Yakunin, M. I. Bodnarchuk, M. J. Grotevent and M. V. Kovalenko, *Nano Letters*, 2015, **15**, 5635-5640.

46. D. M. Jang, K. Park, D. H. Kim, J. Park, F. Shojaei, H. S. Kang, J.-P. Ahn, J. W. Lee and J. K. Song, *Nano Letters*, 2015, **15**, 5191-5199.

47. D. H. Son, S. M. Hughes, Y. Yin and A. Paul Alivisatos, *Science*, 2004, **306**, 1009-1012.

48. R. D. Robinson, B. Sadtler, D. O. Demchenko, C. K. Erdonmez, L.-W. Wang and A. P. Alivisatos, *Science*, 2007, **317**, 355-358.

49. E. M. Chan, M. A. Marcus, S. Fakra, M. ElNaggar, R. A. Mathies and A. P. Alivisatos, *The Journal of Physical Chemistry A*, 2007, **111**, 12210-12215.

50. B. Sadtler, D. O. Demchenko, H. Zheng, S. M. Hughes, M. G. Merkle, U. Dahmen, L.-W. Wang and A. P. Alivisatos, *Journal of the American Chemical Society*, 2009, **131**, 5285-5293.

51. A. M. Smith and S. Nie, *Journal of the American Chemical Society*, 2011, **133**, 24-26.

52. P. K. Jain, B. J. Beberwyck, L.-K. Fong, M. J. Polking and A. P. Alivisatos, *Angewandte Chemie International Edition*, 2012, **51**, 2387-2390.

53. S. L. White, J. G. Smith, M. Behl and P. K. Jain, *Nature Communications*, 2013, **4**, 2933.

54. A. L. Routzahn and P. K. Jain, *Nano Letters*, 2014, **14**, 987-992.

55. A. L. Routzahn and P. K. Jain, *Nano Letters*, 2015, **15**, 2504-2509.

Journal of Materials Chemistry C Accepted Manuscript

View Article Online
DOI: 10.1039/C8TC06470A

Published on 27 February 2019. Downloaded by Washington University in St. Louis on 2/27/2019 4:05:23 PM.

56. S. A. Empedocles, D. J. Norris and M. G. Bawendi, *Physical Review Letters*, 1996, **77**, 3873-3876.

57. M. Nirmal, B. O. Dabbousi, M. G. Bawendi, J. J. Macklin, J. K. Trautman, T. D. Harris and L. E. Brus, *Nature*, 1996, **383**, 802-804.

58. C. Galland, Y. Ghosh, A. Steinbrück, M. Sykora, J. A. Hollingsworth, V. I. Klimov and H. Htoon, *Nature*, 2011, **479**, 203-207.

59. N. J. Orfield, J. R. McBride, J. D. Keene, L. M. Davis and S. J. Rosenthal, *ACS Nano*, 2015, **9**, 831-839.

60. N. J. Orfield, S. Majumder, J. R. McBride, F. Yik-Ching Koh, A. Singh, S. J. Bouquin, J. L. Casson, A. D. Johnson, L. Sun, X. Li, C.-K. Shih, S. J. Rosenthal, J. A. Hollingsworth and H. Htoon, *ACS Nano*, 2018, **12**, 4206-4217.

61. W. Xu, J. S. Kong, Y.-T. E. Yeh and P. Chen, *Nature Materials*, 2008, **7**, 992-996.

62. X. Zhou, N. M. Andoy, G. Liu, E. Choudhary, K.-S. Han, H. Shen and P. Chen, *Nature Nanotechnology*, 2012, **7**, 237-241.

63. Y. Hassan, Y. Song, R. D. Pensack, A. I. Abdelrahman, Y. Kobayashi, M. A. Winnik and G. D. Scholes, *Advanced Materials*, 2016, **28**, 566-573.

64. L. C. Schmidt, A. Pertegás, S. González-Carrero, O. Malinkiewicz, S. Agouram, G. Mínguez Espallargas, H. J. Bolink, R. E. Galian and J. Pérez-Prieto, *Journal of the American Chemical Society*, 2014, **136**, 850-853.

65. W. M. Haynes and D. R. Lide, *CRC Handbook of Chemistry and Physics*, CRC Press, Boca Raton, FL, 2011.

66. D. Pan, Y. Fu, J. Chen, K. J. Czech, J. C. Wright and S. Jin, *Nano Letters*, 2018, **18**, 1807-1813.

Journal of Materials Chemistry C Accepted Manuscript

View Article Online
DOI: 10.1039/C8TC06470A

67. B. Yin, B. Sadtler, M. Y. Berezin and E. Thimsen, *Chemical Communications*, 2016, **52**, 11127-11130.

68. D. W. deQuilettes, S. Koch, S. Burke, R. K. Paranji, A. J. Shropshire, M. E. Ziffer and D. S. Ginger, *ACS Energy Letters*, 2016, **1**, 438-444.

Published on 27 February 2019. Downloaded by Washington University in St. Louis on 2/27/2019 4:05:23 PM.

Journal of Materials Chemistry C Accepted Manuscript

View Article Online
DOI: 10.1039/C8TC06470A

Published on 27 February 2019. Downloaded by Washington University in St. Louis on 2/27/2019 4:05:23 PM.

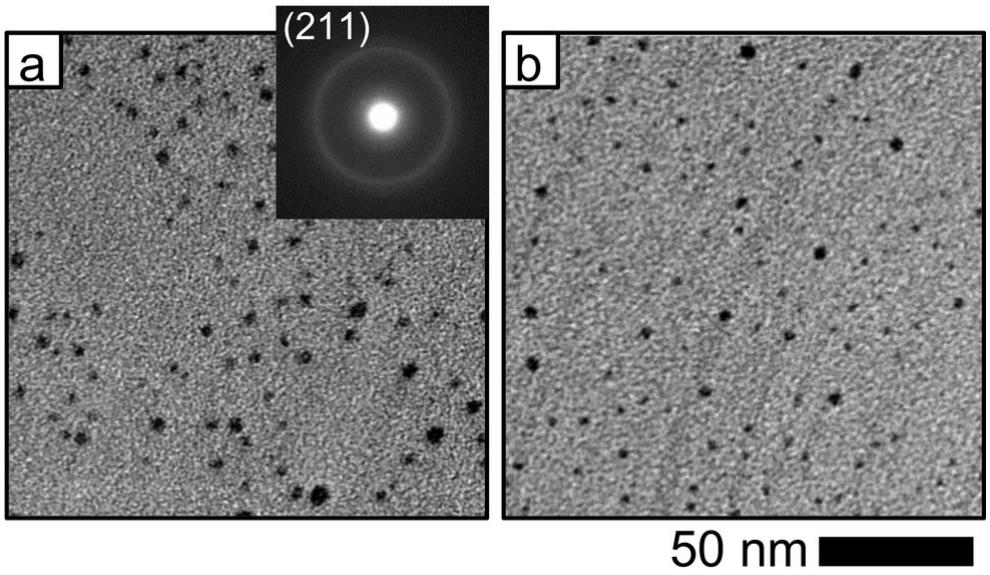

Figure 1. TEM images of (a) the initial $PbBr_2$ nanocrystals and (b) resulting $CH_3NH_3PbBr_3$ nanocrystals after reaction with CH_3NH_3Br. The inset (a) shows an electron diffraction pattern for a cluster of $PbBr_2$ nanocrystals. The bright ring corresponds to the d-spacing for the (211) plane of $PbBr_2$. The scale bar of 50 nm applies to both images.

84x52mm (300 x 300 DPI)

Journal of Materials Chemistry C Accepted Manuscript

View Article Online
DOI: 10.1039/C8TC06470A

Published on 27 February 2019. Downloaded by Washington University in St. Louis on 2/27/2019 4:05:23 PM.

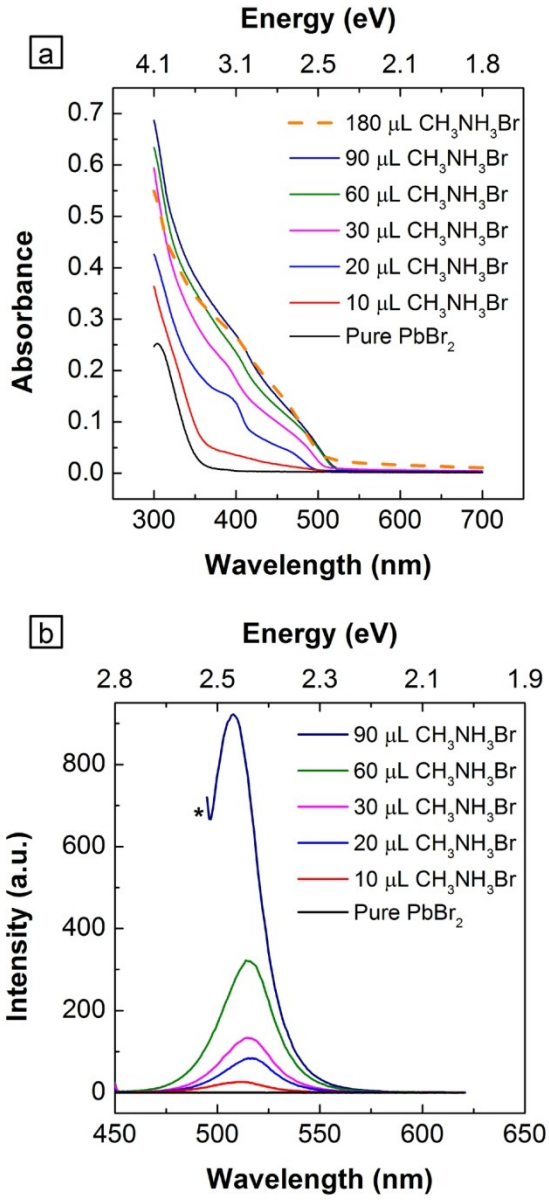

Figure 2. Optical spectra showing the conversion of $PbBr_2$ nanocrystals to $CH_3NH_3PbBr_3$. (a) Absorption spectra of the nanocrystals after the addition of increasing amounts of CH_3NH_3Br. (b) Photoluminescence spectra of the nanocrystals after the addition of increasing amounts of CH_3NH_3Br. The excitation wavelength was 400 nm for all samples except for the 90 μL aliquot in which the excitation wavelength was increased to 475 nm to reduce the emission intensity.

80x175mm (300 x 300 DPI)

Journal of Materials Chemistry C Accepted Manuscript

View Article Online
DOI: 10.1039/C8TC06470A

Published on 27 February 2019. Downloaded by Washington University in St. Louis on 2/27/2019 4:05:23 PM.

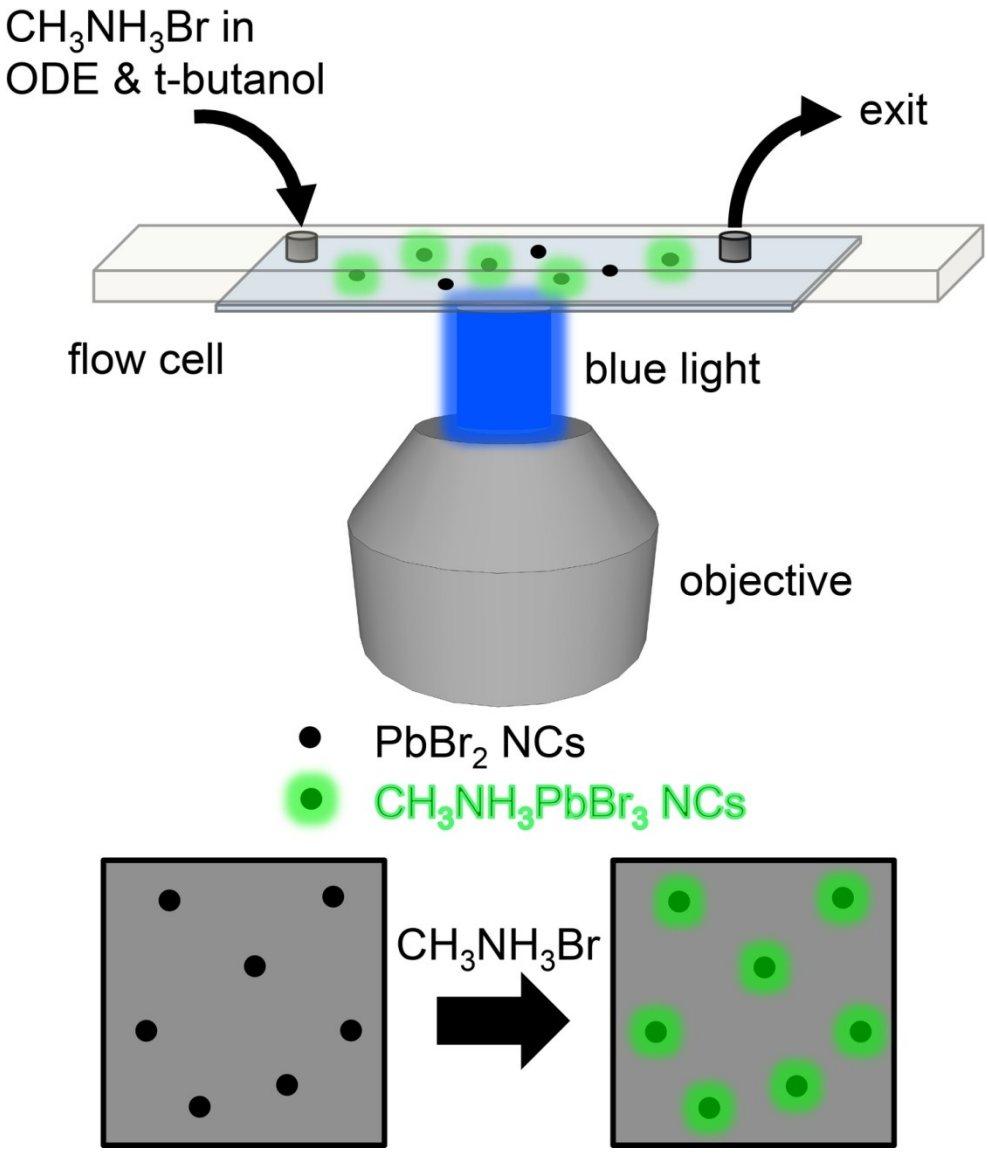

Scheme 1. Experimental Configuration Used to Observe the Transformation of Single $PbBr_2$ Nanocrystals to $CH_3NH_3PbBr_3$. Upon excitation with blue light (450 to 480 nm), the initial $PbBr_2$ nanocrystals are non-fluorescent while the product $CH_3NH_3PbBr_3$ nanocrystals are highly fluorescent. A schematic of the microscope field-of-view is shown at the bottom. Black dots represent $PbBr_2$ nanocrystals, and green dots represent $CH_3NH_3PbBr_3$ nanocrystals after the transformation. ODE = 1-octadecene.

128x148mm (300 x 300 DPI)

Journal of Materials Chemistry C Accepted Manuscript

View Article Online
DOI: 10.1039/C8TC06470A

Published on 27 February 2019. Downloaded by Washington University in St. Louis on 2/27/2019 4:05:23 PM.

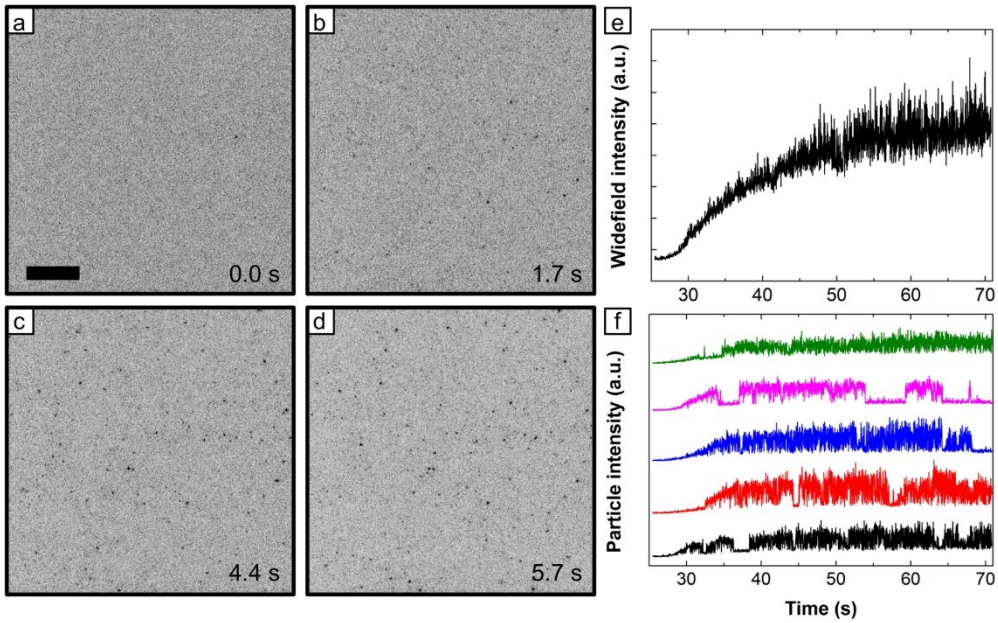

Figure 3. Imaging the transformation of single $PbBr_2$ nanocrystals to $CH_3NH_3PbBr_3$. (a-d) Selected frames from a video recording of the fluorescence intensity under excitation with blue light and using a CH_3NH_3Br concentration of 0.4 mg/mL. The first frame (0.0 sec) corresponds to the time when the first fluorescent spot appeared. The contrast of the images has been inverted. The scale bar shown in (a) is 5 μm and applies to all four images. (e) The integrated intensity versus time over the entire field-of-view for the same recording. (f) Intensity trajectories for individual nanocrystals from the same recording.

165x102mm (300 x 300 DPI)

Journal of Materials Chemistry C Accepted Manuscript

View Article Online
DOI: 10.1039/C8TC06470A

Published on 27 February 2019. Downloaded by Washington University in St. Louis on 2/27/2019 4:05:23 PM.

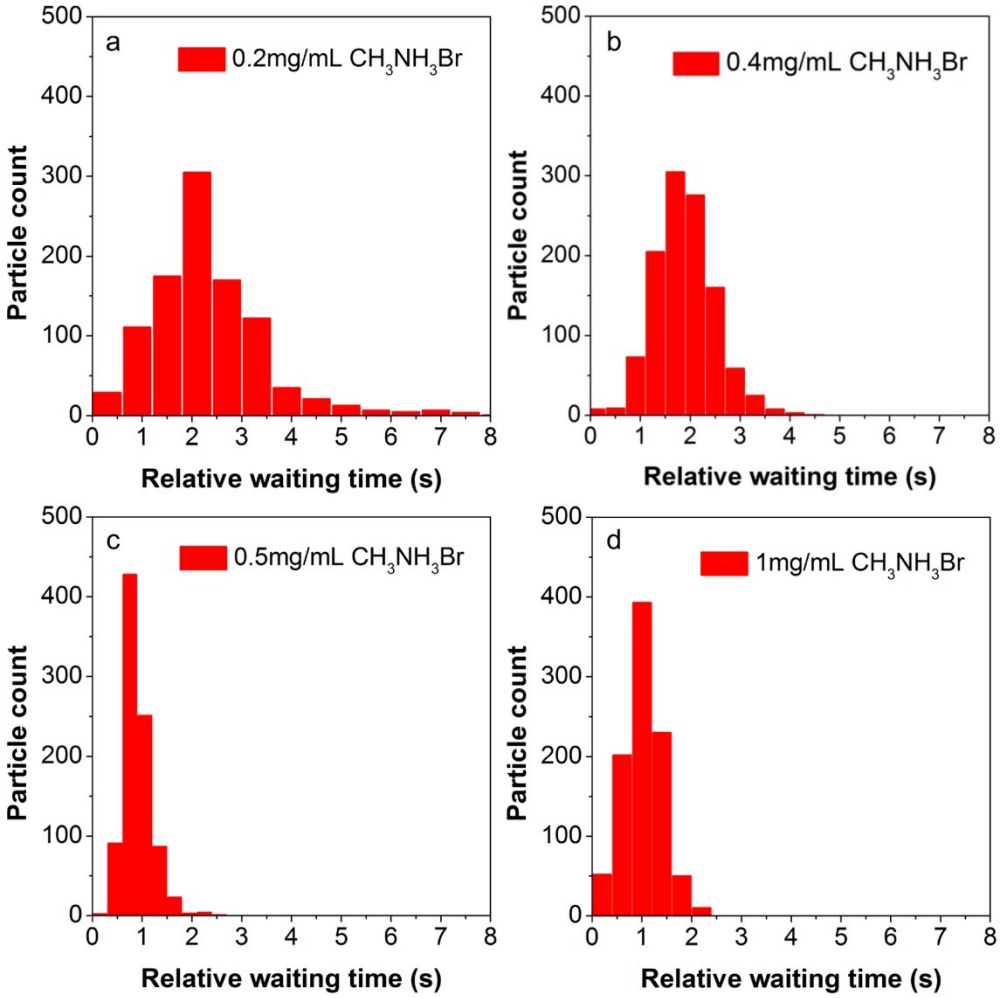

Figure 4. Histograms of the relative waiting times for $PbBr_2$ nanocrystals to transform into $CH_3NH_3PbBr_3$ when the concentration of CH_3NH_3Br was (a) 0.2 mg/mL, (b) 0.4 mg/mL, (c) 0.5 mg/mL, and (d) 1.0 mg/mL. For each histogram, a relative waiting time of 0 seconds corresponds to the first nanocrystal to transform among the population. The ESI describes how histograms were aligned when multiple videos were recorded at the same concentration.

152x151mm (300 x 300 DPI)

Journal of Materials Chemistry C Accepted Manuscript

View Article Online
DOI: 10.1039/C8TC06470A

Published on 27 February 2019. Downloaded by Washington University in St. Louis on 2/27/2019 4:05:23 PM.

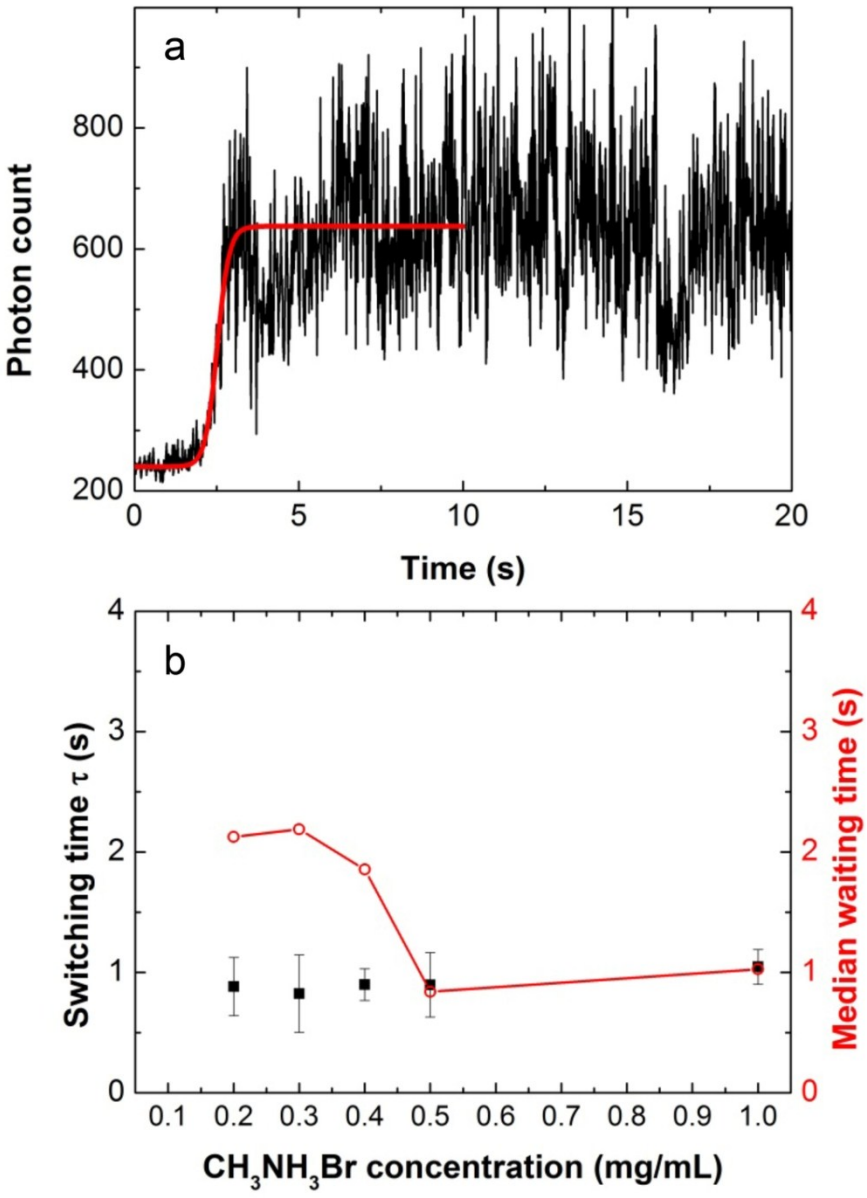

Figure 5. (a) Representative intensity trajectory (black trace) for a single nanocrystal and the fitting (red line) of the intensity rise to a sigmoidal function. This fitting was used to determine the switching time, τ. (b) The average switching time (black squares) and the median relative waiting time (red circles) for the conversion of $PbBr_2$ nanocrystals using different CH_3NH_3Br concentrations. The error bars for the average switching times correspond to one standard deviation.

89x123mm (300 x 300 DPI)

Journal of Materials Chemistry C Accepted Manuscript

View Article Online
DOI: 10.1039/C8TC06470A

Published on 27 February 2019. Downloaded by Washington University in St. Louis on 2/27/2019 4:05:23 PM.

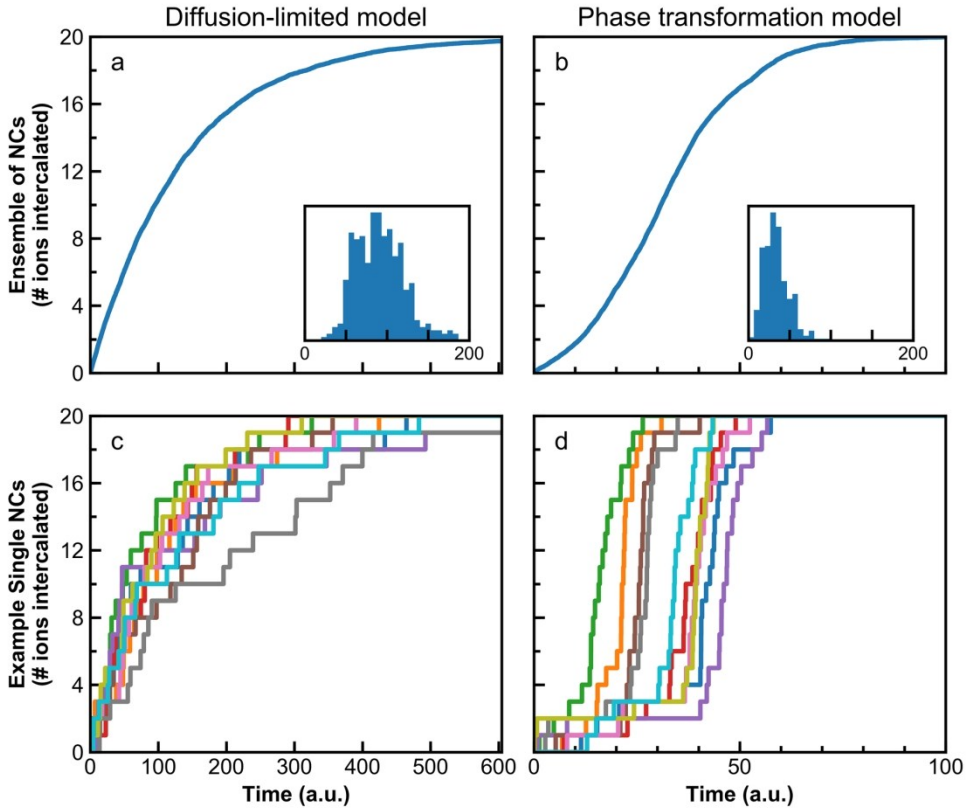

Figure 6. Monte Carlo simulations of ion intercalation in $PbBr_2$ nanocrystals. Ensemble reaction trajectories for the (a) diffusion-limited and (b) phase-transformation models described in the text. The insets show histograms of the waiting times for individual trajectories using these models. Representative single-particle trajectories for the (c) diffusion-limited and (d) phase-transformation models.

165x139mm (300 x 300 DPI)

Journal of Materials Chemistry C Accepted Manuscript